Revista Mexicana de Astronomía y Astrofísica, **36**, 67–76 (2000)

A NEW, 3D ADAPTIVE GRID CODE FOR ASTROPHYSICAL AND GEOPHYSICAL GASDYNAMICS

A. C. Raga,[1] R. Navarro-González,[2] and M. Villagrán-Muniz[3]

Received 2000 March 10; accepted 2000 March 31

RESUMEN

Este trabajo describe un nuevo código tridimensional de red adaptativa, que resuelve las ecuaciones de la dinámica de gases, junto con un sistema de ecuaciones para la evolución de especies atómicas/iónicas y moleculares. Este código también incluye un tratamiento del transporte radiativo, que fue desarrollado para un código anterior de red uniforme.

Para validar el código, presentamos una comparación entre una simulación numérica y un experimento de laboratorio de una onda de choque empujada por una burbuja de plasma generada con un laser de Nd:YAG. Encontramos un acuerdo muy bueno entre la evolución temporal de la onda de choque medida experimentalmente, y la obtenida de la simulación numérica.

Finalmente, se discuten las aplicaciones futuras de este código a problemas astrofísicos y geofísicos.

ABSTRACT

This paper describes a new, 3D adaptive grid code which solves the gasdynamic equations together with a system of rate equations for atomic/ionic and molecular species. This code also includes a treatment of the radiative transfer, which had been developed for a previous, uniform grid 3D code.

In order to validate the code, we present a comparison between a numerical simulation and a laboratory experiment of a shock wave driven by a Nd:YAG laser-generated, expanding plasma bubble. We find that the agreement between the predicted and observed time-evolution of the shock wave is highly satisfactory.

Finally, future applications of this code to astrophysical and geophysical problems are discussed.

Key words: **HYDRODYNAMICS — SHOCK WAVES**

1. INTRODUCTION

Over the last two decades, adaptive grid methods have been incorporated into astrophysical gasdynamic codes. This has been done for 2D codes (Falle & Giddings 1993; Klein, McKee, & Colella 1994) and more recently for 3D codes (Truelove et al. 1998; Lim & Steffen 2000). Two-dimensional (plane or axisymmetric), adaptive grid gasdynamic models have also been computed including detailed treatments of the non-equilibrium ionization (Raga, Mellema, & Lundqvist 1997b) and chemistry (Lim, Rawlings, & Williams 1999) of the gas, as well as a treatment of the transfer of the ionizing radiation (Mellema et al. 1998; Williams 1999).

In the present paper, we discuss the characteristics of a newly developed, 3D adaptive grid code. This code solves the gasdynamic equations with the "flux vector splitting" algorithm of Van Leer (1982), and also solves a system of rate equations for atomic/ionic and molecular species with a fast, semi-implicit method. Both the numerical method (§ 2 and § 4) and the characteristics of the adaptive grid (§ 3) are discussed in detail.

[1] Instituto de Astronomía, Universidad Nacional Autónoma de México.
[2] Instituto de Ciencias Nucleares, Universidad Nacional Autónoma de México.
[3] Centro de Instrumentos, Universidad Nacional Autónoma de México.

In order to test the code, we carry out a comparison between a numerical simulation and the results of a laboratory experiment. In this experiment, a high pressure plasma bubble is generated close to the focal point of a focused Nd:YAG laser beam. This bubble then expands, driving a non-spherical shock wave into the surrounding atmosphere. The shape of this shock wave is measured as a function of time, and these measurements are directly compared with the numerical solution produced with our 3D code (§ 5). This experiment is of general interest as a test for astrophysically oriented gasdynamic codes.

2. GASDYNAMIC METHOD

The new yguazú-a code integrates a system of equations consisting of the 3D gasdynamic (Euler) equations, and a series of rate equations for atomic/ionic or molecular species. This system can be written as

$$\frac{\partial U}{\partial t} + \frac{\partial F}{\partial x} + \frac{\partial G}{\partial y} + \frac{\partial H}{\partial z} = S\,, \tag{1}$$

where

$$U = [E,\, \rho u,\, \rho v,\, \rho e,\, \rho,\, n_1,\, n_2, ...n_R]\,, \tag{2}$$

$$F = \left[u(E+P), \rho u^2 + P, \rho uv, \rho uw, \rho u, n_1 u, ...n_R u\right]\,, \tag{3}$$

$$G = \left[v(E+P), \rho uv, \rho v^2 + P, \rho vw, \rho v, n_1 v, ...n_R v\right]\,, \tag{4}$$

$$H = \left[w(E+P), \rho uw, \rho vw, \rho w^2 + P, \rho w,\, n_1 w, ...n_R w\right]\,, \tag{5}$$

$$S = [G - L,\, 0,\, 0,\, 0,\, 0,\, S_1,\, S_2,\, ...S_R]\,, \tag{6}$$

with

$$E = \frac{1}{2}\rho(u^2 + v^2 + w^2) + C_v P\,, \tag{7}$$

$$P = \left(\frac{\rho}{m} + n_e\right) kT\,, \tag{8}$$

$$n_e = \sum_{r=1}^{R} z_r n_r\,, \tag{9}$$

$$m = \frac{\sum_{r=1}^{R} m_r n_r}{\sum_{r=1}^{R} n_r}\,, \tag{10}$$

in which (u, v, w) are the three components of the flow velocity along the (x, y, z)-directions, ρ is the density, P the pressure, T the temperature, and n_1, n_2, ...n_R are the number densities of the atomic/ionic and molecular species which have masses $m_1, ...m_R$ and charges $z_1, ...z_R$.

The specific heat at constant volume C_v is approximated as

$$C_v = \frac{3n_{at} + 5n_{mol}}{2(n_{at} + n_{mol})}\,, \tag{11}$$

where n_{at} is the number density of atoms and ions, and n_{mol} is the number density of molecules. This is of course only a simple approximation to the much more complex behaviour of the specific heat of a mixture of an atomic/ionic and a molecular gas (see, e.g., Flower & Pineau des Fôrets 1999; Horváth & Ziegler 1999).

Finally, the source vector S (see equation 6) includes the energy gain by photoionization G and the energy loss L, and the source terms $S_1, ...S_R$ due to reactions between the different species. The source vector can easily be extended to include geometrical source terms for cylindrical and spherical coordinate systems.

The system of equations (1) is advanced in time in the following way. A first-order half-timestep is computed as

$$U_{ijk}(t+\frac{\Delta t}{2}) = U_{ijk}(t)$$
$$-\frac{\Delta t}{2\Delta x}\left(F^{+}{}_{i-1,j,k} + F^{-}{}_{i+1,j,k} - F^{+}{}_{ijk} - F^{-}{}_{ijk}\right)$$
$$-\frac{\Delta t}{2\Delta y}\left(G^{+}{}_{i,j-1,k} + G^{-}{}_{i,j+1,k} - G^{+}{}_{ijk} - G^{-}{}_{ijk}\right)$$
$$-\frac{\Delta t}{2\Delta z}\left(H^{+}{}_{i,j,k-1} + H^{-}{}_{i,j,k+1} - H^{+}{}_{ijk} - H^{-}{}_{ijk}\right)$$
$$+\frac{\Delta t}{2} < S >_{ijk}(t)\,, \tag{12}$$

where i, j, k and Δx, Δy, Δz are the indices and grid spacings associated with the x, y and z coordinate axes (respectively), and the fluxes F^{+}, F^{-}, G^{+}, G^{-}, H^{+} and H^{-} are calculated according to the "flux vector splitting" algorithm of Van Leer (1982) with the values of $U(t)$ (at cell centre).

With the updated $U(t+\Delta t/2)$ we then compute the primitive variables $Prim(t+\Delta t/2)$, where

$$Prim = [P,\, u,\, v,\, w,\, \rho,\, n_1,\, ...n_R]\,. \tag{13}$$

With the primitive variables we compute the gradients along the three coordinate axes, to each side of point (i,j,k):

$$\Delta^{+}{}_{x,ijk} = Prim_{i+1,j,k} - Prim_{ijk}\,, \tag{14}$$

$$\Delta^{-}{}_{x,ijk} = Prim_{ijk} - Prim_{i-1,j,k}\,, \tag{15}$$

$$\Delta^{+}{}_{y,ijk} = Prim_{i,j+1,k} - Prim_{ijk}\,, \tag{16}$$

$$\Delta^{-}{}_{y,ijk} = Prim_{ijk} - Prim_{i,j-1,k}\,, \tag{17}$$

$$\Delta^{+}{}_{z,ijk} = Prim_{i,j,k+1} - Prim_{ijk}\,, \tag{18}$$

$$\Delta^{-}{}_{z,ijk} = Prim_{ijk} - Prim_{i,j,k-1}\,, \tag{19}$$

and the gradients within each grid cell as

$$\Delta_x = Av\left(\Delta^{+}{}_x,\, \Delta^{-}{}_x\right) \tag{20}$$

$$\Delta_y = Av\left(\Delta^{+}{}_y,\, \Delta^{-}{}_y\right) \tag{21}$$

$$\Delta_z = Av\left(\Delta^{+}{}_z,\, \Delta^{-}{}_z\right) \tag{22}$$

with the averaging function

$$Av(A,\,B) = 0\,;\;\; A.B \le 0\,,$$
$$Av(A,\,B) = \frac{A\,B^2 + B\,A^2}{A^2 + B^2}\,;\;\; A.B > 0\,, \tag{23}$$

The primitive variables (at $t + \Delta t/2$) can then be extrapolated to the cell boundaries:

$$Prim_{i-1/2,j,k} = Prim_{ijk} - \frac{\Delta_{x,ijk}}{2}\,, \tag{24}$$

$$Prim_{i+1/2,j,k} = Prim_{ijk} + \frac{\Delta_{x,ijk}}{2}\,, \tag{25}$$

with analogous expressions for the cell boundaries along the y- and z-axes. With these variables, we can then compute the fluxes at the cell boundaries, in order to carry out the full, second order timestep:

$$\begin{aligned} U_{ijk}(t+\Delta t) = U_{ijk}(t) \\ -\frac{\Delta t}{\Delta x}\left(F^{+}{}_{(i-1)+1/2,j,k} + F^{-}{}_{(i+1)-1/2,j,k} - F^{+}{}_{ijk} - F^{-}{}_{ijk}\right) \\ -\frac{\Delta t}{\Delta y}\left(G^{+}{}_{i,(j-1)+1/2,k} + G^{-}{}_{i,(j+1)-1/2,k} - G^{+}{}_{ijk} - G^{-}{}_{ijk}\right) \\ -\frac{\Delta t}{\Delta z}\left(H^{+}{}_{i,j,(k-1)+1/2} + H^{-}{}_{i,j,(k+1)-1/2} - H^{+}{}_{ijk} - H^{-}{}_{ijk}\right) \\ +\Delta t < S >_{ijk}(t)\,. \end{aligned} \tag{26}$$

The source terms $< S >$ averaged over the timestep are computed with a semi-implicit method which is described in § 4.

3. THE ADAPTIVE GRID

The gasdynamic+rate equations are integrated on an adaptive, binary, heirarchical computational grid. The characteristics of the 3D grid are described in the following.

- **Base grid**: There are two grids, $g = 1$ and $g = 2$, which are defined over the whole computational domain. The grid spacings along the three coordinate axes of grid $g = 2$ are a factor of 2 smaller than the corresponding spacings of grid $g = 1$.
- **Timestep**: the timestep is chosen with the appropriate Courant condition, and the successive grids are marched forward in time with timesteps which differ by factors of 2. The timestep for grid g is therefore related to the one of the next lowest resolution grid through $\Delta t_g = \Delta t_{g-1}/2$. After stepping grid g forward in time twice, the results are copied over to the points of grid $g - 1$ which spatially coincide with points of grid g.
- **Refinements on roundoff error**: As an estimate of the roundoff error, we use the difference between the values at a given spatial position obtained in two successive grids g and $g - 1$. If at a given time the integrated flow variables obtained for any of the vertices of a cube (of consecutive points) in the g grid differ from the results obtained in the $g - 1$ grid (for the points defined on both grids) by a fractional amount greater than a fixed lower limit ϵ, the vertices of the cube are copied over to a higher resolution grid $g + 1$ (unless this region of the computational domain is already defined in the $g + 1$ grid). The missing points in the region of the $g + 1$ grid contained within the cube are created through linear interpolations between the values at the vertices of the g grid cube (see Figure 1).
- **Refinement on proximity of higher resolution grid**: If any of the vertices of a cube in grid g or any of the vertices of the adjacent cubes (see Fig. 1) is defined in grid $g + 2$, the cube is then copied over and interpolated into grid $g + 1$ (unless the region of the domain is already defined in $g + 1$).
- **Other refinement criteria**: It is straightforward to introduce other refinement criteria. For example, one can limit some of the grid refinements to a chosen spatial region, or to a given Lagrangean region of the fluid (which can be labeled with a passive scalar). Also, one can refine on the value of any of the flow variables, or on their gradients.
- **Derefinements**: When the refinement criteria are not met, the corresponding grid points are deleted.
- **Grid boundaries**: In carrying out each timestep in grid g, it is necessary to use the values of the neighbouring points in the grid. If these points do not exist, the values for the appropriate position are computed by linearly interpolating the primitive variables (see equation 13) in both space and time between the appropriate points of grid $g - 1$.

With the points discussed above, one can construct a 3D grid system in which the whole domain is defined

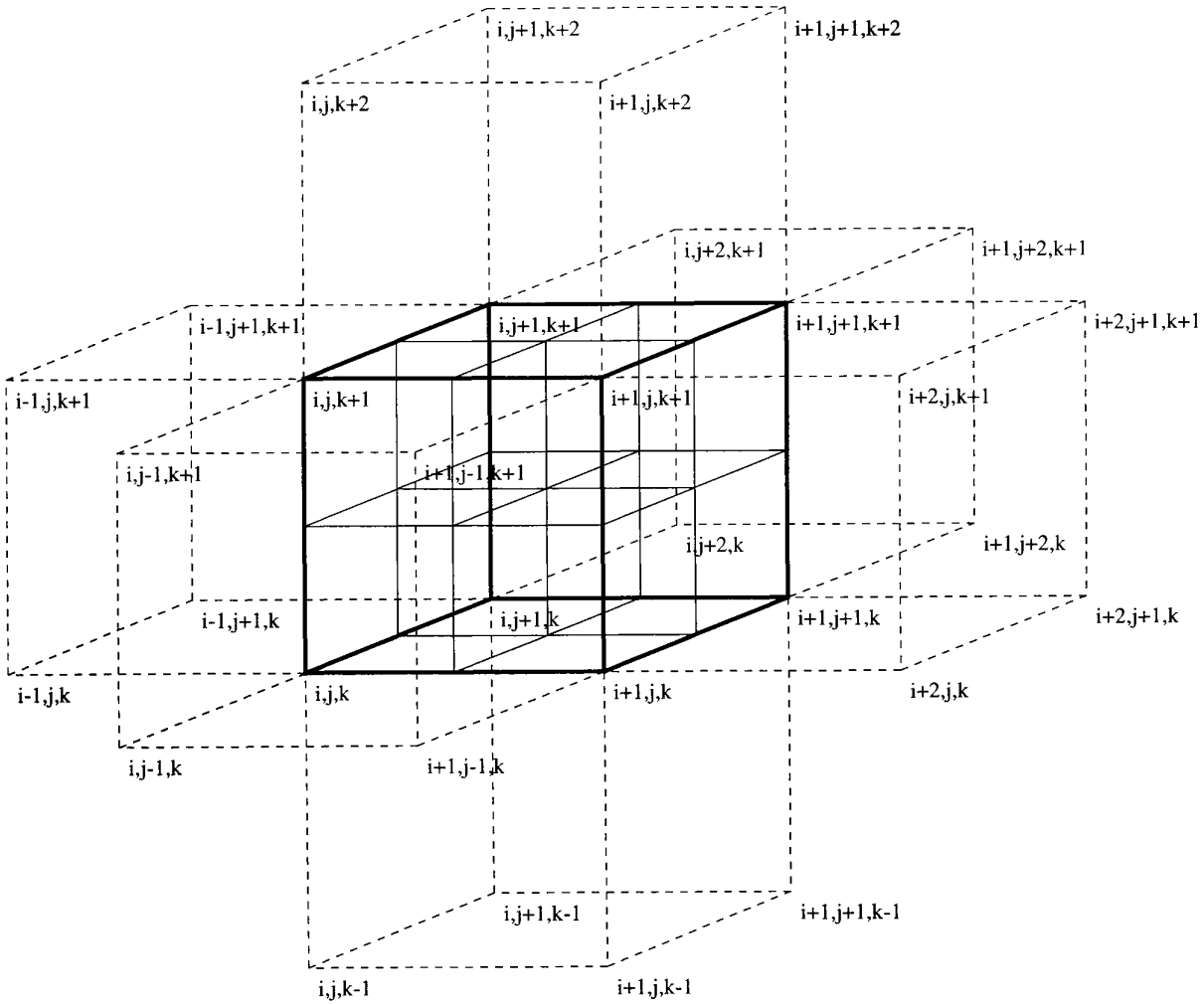

Fig. 1. Schematic diagram showing a cube in grid g (with vertex i, j, k closest to the origin of the coordinate system), and the contiguous cubes of grid g. The thin, solid lines show the geometry of the points to be generated on refinement to grid $g + 1$. Eight of the grid $g + 1$ points coincide with the vertices of the grid g cube. Twelve of the grid $g + 1$ points lie along the edges of the grid g cube (e.g., point $i + 1/2, j, k$) and are asigned flow variables corresponding to the straight average of the primitive variables at the contiguous vertices. Six grid $g + 1$ points lie on the centre of each of the sides of the cube, and are asigned values corresponding to the average of the four vertices of the cube side. Finally, there is one grid $g + 1$ point at the centre of the cube, to which we asign the average of the 8 vertices of the grid g cube.

in two grids ($g = 1$ and 2, with a factor of 2 resolution difference along the three axes), and with smaller regions of the domain being defined in higher resolution grids ($g = 4, 5, ...g_{max}$) with successive factor of 2 increases in resolution.

We should note that the characteristics of this adaptive grid are similar to the ones of the Cobra code (see, e.g., Falle & Giddings 1993; Falle & Raga 1993). However, it is not possible to evaluate the differences between the two codes as the details of the adaptive grid of the Cobra code have not been published.

4. REACTION SOURCE TERMS

In order to integrate the system of atomic/ionic and molecular rate equations (see eqs. 1 and 6), we use a semi-implicit method inspired in the work of Young & Boris (1973), which places no requirements on the value of the timestep.

Let us consider three species, A, B, and C, which are connected through a reaction $A + B \rightarrow C$. We then assume that within each timestep Δt the reaction rate can be written as

$$S = n_A n_B q \ , \tag{27}$$

with constant q. The rate equations (not considering the advection terms nor other reactions involving some of the same species) for the number densities n_A and n_B are then

$$\frac{dn_A}{dt} = -n_A n_B q \ , \tag{28}$$

$$\frac{dn_B}{dt} = -n_A n_B q \ . \tag{29}$$

If $n_B \gg n_A$, we can consider $n_B \approx const.$ in equation (28), and integrate within the timestep Δt to obtain:

$$n_A(t + \Delta t) = n_A(t)\, e^{-n_B q \Delta t} \ , \tag{30}$$

from which we can calculate a value for the source term averaged over the Δt time interval:

$$S_A(t, \Delta t) = \frac{n_A(t + \Delta t) - n_A(t)}{\Delta t} = \frac{n_A(t)}{\Delta t} \left(1 - e^{-n_B q \Delta t}\right) \ . \tag{31}$$

Analogously, for the $n_A \gg n_B$ case, from equation (29) we obtain:

$$S_B(t, \Delta t) = \frac{n_B(t)}{\Delta t} \left(1 - e^{-n_A q \Delta t}\right) \ . \tag{32}$$

We then define the average value for the source term within Δt as:

$$< S > (t, \Delta t) = Av(S_A, S_B) \, , \tag{33}$$

using the averaging function defined in equation (23), which gives a value close to the smaller of the two arguments.

In general, the full rate equation for species r can be written as a sum over a series of two-species reactions:

$$\frac{dn_r}{dt} = -\sum_{p \neq r} n_p n_r q_{pr} + \sum_{p,s} n_p n_s q^{(r)}{}_{ps} \ , \tag{34}$$

where q_{pr} are the rate coefficients for reactions in which species r is destroyed, and $q^{(r)}{}_{ps}$ correspond to reactions (between species p and s) which form species r. We now choose a timestep $\Delta t_c = \Delta t / N_c$, where Δt is the timestep fixed by the gasdynamic Courant criterion, and N_c is an integer of the same order as the number of reactions per species in the reaction network. We then perform N_c timesteps of length Δt_c with the algorithm:

$$n_r(t_n) = -\Delta t_c \sum_{p \neq r} < S_{pr} > (t_{n-1}, \Delta t) + \Delta t_c \sum_{p,s} < S^{(r)}{}_{ps} > (t_{n-1}, \Delta t) \, , \tag{35}$$

where $t_n = t + n \Delta t_c$ (with $n = 1, ...N_c$) and the average rates are given by equations (31–33). This algorithm is stable for any chosen Δt, and gives the correct convergence to partial equilibria between species resulting from fast reactions.

Finally, for the source term of the energy equation (see equations 12 and 26), we assume that within Δt the fluid parcels cool at constant density, that the heating rate G is constant, and that the cooling rate is proportional to the temperature. It is straightforward to show that under these assumptions one obtains:

$$< G - L > (t, \Delta t) = C_v \frac{P_{eq} - P(t)}{\Delta t} \left(1 - e^{-\Delta t / t_{rel}}\right) , \tag{36}$$

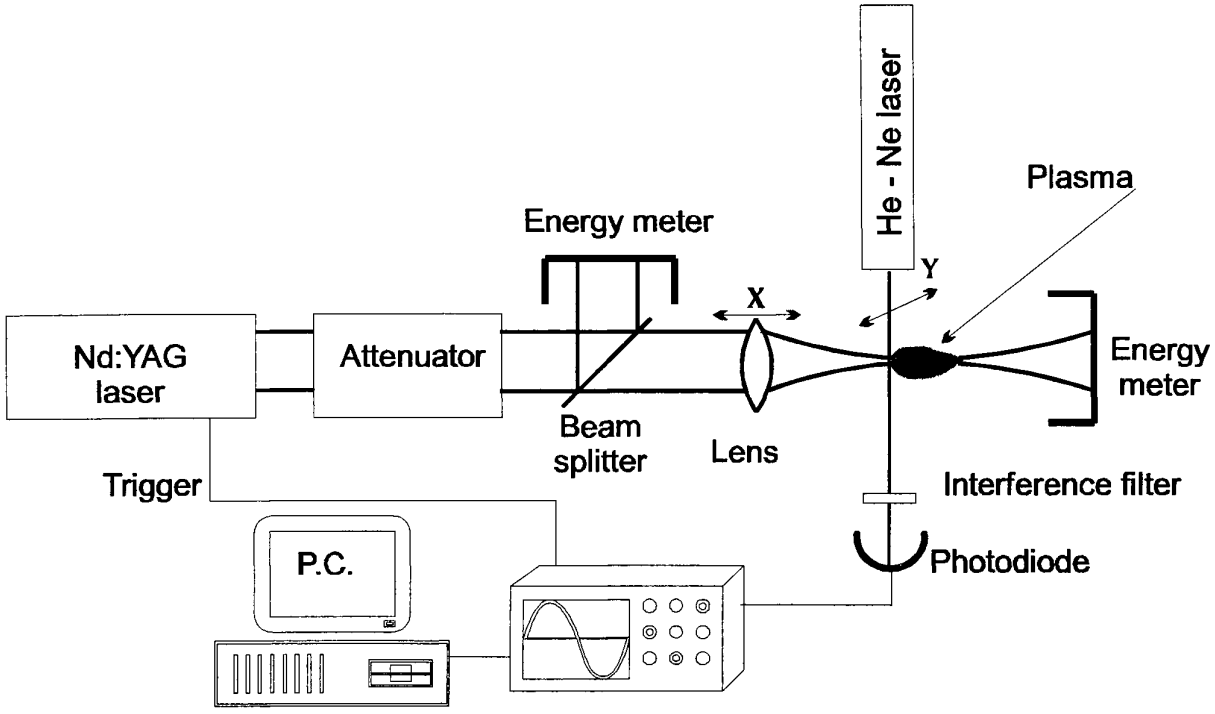

Fig. 2. Experimental setup for generating a laser-induced plasma bubble in air and for measuring the locus of the resulting shock wave. A Nd:YAG laser beam (1.06 μm, 7 ns, 10 Hz) is focused with a plano-convex lens (5 cm focal length with anti-reflection coating). A partially ionized, high pressure plasma bubble is produced at the focal point at atmospheric conditions in México City ($\rho \approx 10^{-3}$ g cm^{-3}). The expanding bubble drives a shock wave, which is detected by measuring the deflection signal of a probe beam HeNe laser (1 mW, 632 nm, $\phi = 630$ μm). The lens and the probing laser were mounted on micrometric translation stages to vary the sampling position of the shock wave in the x and y axes. The lag between the deflection time and the ignition was then measured in order to map the position of the expanding shock wave as a function of time. The beam deflection was detected by a fast response photodiode (rise time 200 ps) and registered by a 500 MHz digital oscilloscope triggered with an external pulse from the power supply of the Nd:YAG laser. Moving the lens and the probing beam in intervals of 500 μm enabled us to map the shock wave in two dimensions. The signals were stored in a PC with a GPIB interface for subsequent analysis. The energy of the laser pulse was set at 300 mJ using a high power attenuator and was measured before the focusing lens by means of a calibrated beam splitter and after the plasma by a two-head energy meter. In order to avoid detection of laser scattered light (1.06 μm) and plasma emission, the photodiode was covered with an interference filter. Deflection signals were gathered from the average of 25 acquisitions.

where

$$t_{rel} = \frac{C_v P(t)}{L(t)}, \tag{37}$$

$$P_{eq} = \frac{G(t)P(t)}{L(t)}, \tag{38}$$

with t being the initial time for the timestep Δt.

5. COMPARISON WITH PLASMA BUBBLE EXPERIMENT

In order to test the accuracy of the yguazú-a code, we compare a numerical simulation with results from a laboratory experiment. This experiment is as follows.

The experimental setup is shown in Figure 2. A pulse from a Nd:YAG laser with an energy of 300 mJ, and a duration of 7 nanoseconds is focused with a 5 cm focal length lens. An approximately conical region

surrounding the beam convergence cone (see Fig. 2) is partially ionized by the laser pulse (with an ionization fraction of ~ 1 %) and heated to a temperature of $\approx 12,000$ K. This high pressure region then expands, pushing out a shock wave into the surrounding atmosphere.

The position of the shock wave is measured using the photoacoustic probe beam deflection technique (see Fig. 2). This method is based on the deflection of a continuous probe laser beam due the temporal change of the refractive index of air when instantaneously heated by the expanding shock wave. The deflection is measured with a photodiode which sends out a signal to the oscilloscope. The time lag between the deflection signal and plasma ignition is used to construct a two-dimensional plot of the shock wave front by displacing both the focusing lens and the probing laser beam. The shock wave evolution is then studied by searching for the x, y-coordinates of the deflection signal at a given time. The experimental setup is described in detail by Villagrán-Muniz & Navarro-González (2000).

Figure 3 shows the locus of the shock wave for times $t = 3$, 5, and 7 μs after laser-induced breakdown occured. In the same figure we show the results obtained from a numerical simulation carried out with the yguazú-a code.

As the initial conditions for the shape of the plasma bubble are not known in a quantitative way, for the simulation we impose a temperature $T_p = 12,000$ K in a conical region with a (full) opening angle α and length l. The density inside the cone has the same value as the outer, unperturbed atmosphere region (which has a temperature $T_a = 300$ K and density $\rho_a = 10^{-3}$g cm^{-3}). The numerical simulation is carried out for a domain of $2 \times 2 \times 2$ cm, in a grid system with 6 levels of binary grid refinement, with a maximum resolution (along the three axes) of 7.8×10^{-3} cm. It is assumed that the specific heat has a constant, $C_v = 2.5$ value (see equation 11).

We find that if one chooses an initial cone with opening angle $\alpha = 30°$ and length $l = 2.5$ mm, the shape for the shock wave obtained from the numerical simulation agrees with the experimentally determined shock locus for $t = 3$, 5, and 7 μs. As shown in Fig. 3, this agreement is highly satsifactory.

From this comparison, we conclude that the yguazú-a code can reproduce the time-dependent evolution of the shock wave produced by an expanding, laser-generated plasma bubble. With this laboratory experiment, we have also tested a 2D, axisymmetric version of the yguazú-a code, with basically identical results to the ones shown in Figure 3.

6. CONCLUSIONS

We have discussed the characteristics of a new, 3D, binary adaptive grid code that solves the gasdynamic equations together with a system of rate equations for atomic/ionic and/or molecular species. A detailed discussion of the implementation of the "flux vector splitting" algorithm, the adaptive grid and the treatment of the heating/cooling and ionization/chemical source terms has been made.

In the past, we have presented extensive comparisons of codes based on Van Leer's (1982) method with different analytic and numerical solutions (see, e.g., Raga et al. 1997a), and also tests of schemes for the integration of rate equations which are similar to the ones of the present paper (though less general, in that they were specifically aimed at the special form taken by ionization rate of change equations, see Raga et al. 1997b).

We have therefore now chosen to carry out a different type of test, in which we compare the results from a numerical simulation with a laboratory experiment. In particular, we have modeled the expanding shock wave produced by a laser-generated plasma bubble. This experiment provides an excelent opportunity for quantifying the ability of a multidimensional gasdynamic code to track the time evolution of a strong, travelling shock wave.

We find that it is possible to obtain a very good agreement between the shape of the measured and the numerically predicted shock waves. This comparison is quite convincing, and shows that our adaptive grid code produces reliable results.

The yguazú-a code can also integrate the transfer of direct and diffuse radiation, and include the radiative effects on the ionization and molecular reaction rates. We do not include a description of this in the present paper, as detailed descriptions of the radiative transfer (for a previous, uniform grid code) have been presented by Raga et al. (1999) and Raga & Williams (2000). In the near future, we will also implement a solution of the Poisson equation for the gravitational field, which will allow us to compute self-gravitating, astrophysical flows.

With this tool, we will be able to study diverse problems such as 3D jets from time-dependent sources, the formation of multiple stars and giant planets, and tidal and ram pressure stripping of gas from dwarf spheroidal galaxies. For this last problem, we will combine the yguazú-a code with a N-body code which we are currently developing.

Finally, the yguazú-a code also incorporates the possibility of having boundary conditions involving rigid

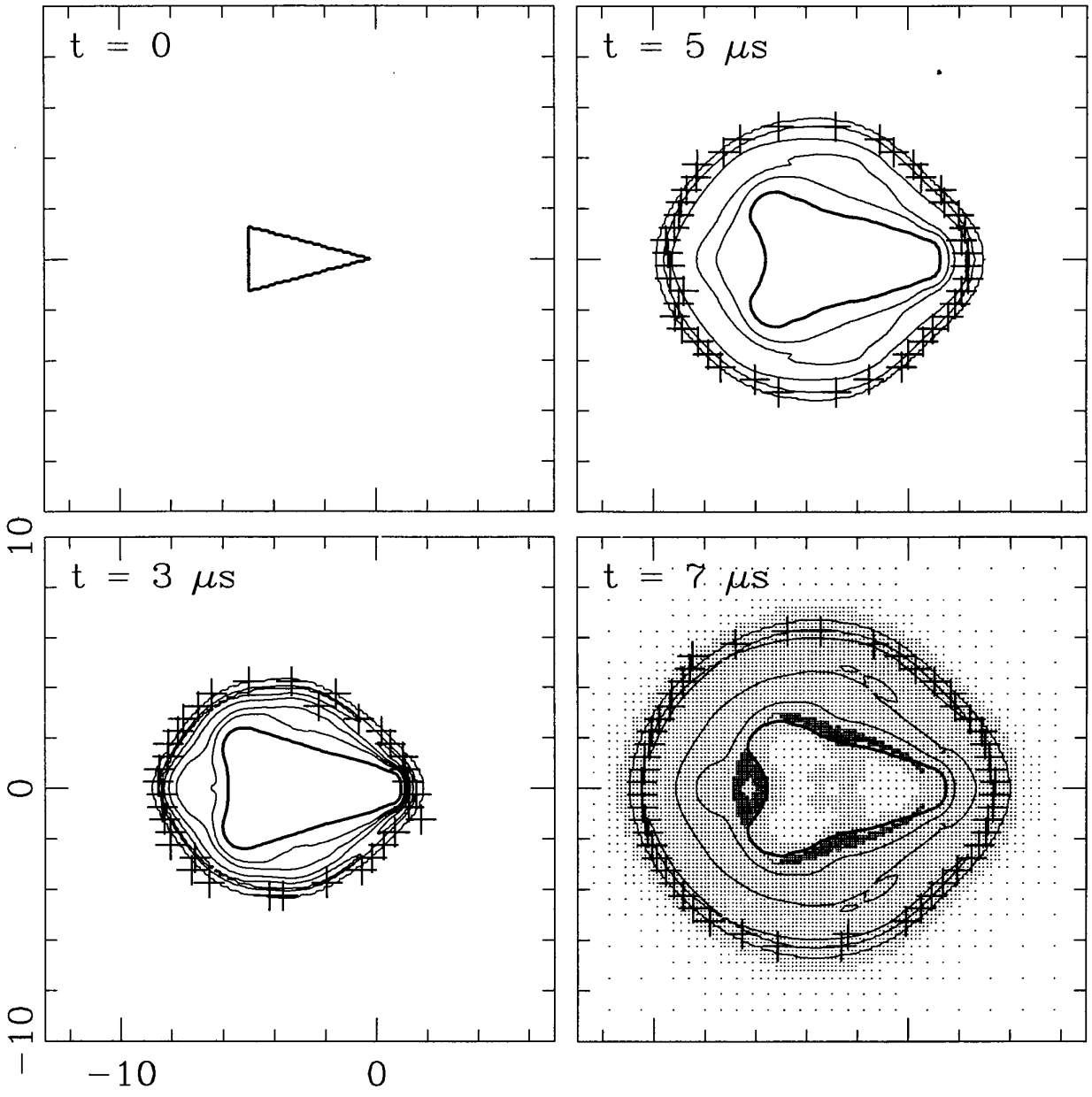

Fig. 3. Comparison of a 3D numerical simulation with the shock wave evolution determined from the plasma bubble experiment. The experimentally determined locci of the shock wave at 3, 5, and 7 μs after the ionizing laser pulse are shown with the crosses. The thin contours represent the density stratification determined for the same times from the numerical simulation (the successive contours corresponding to linear steps of 5×10^{-4} g cm^{-3}), for a cut (parallel to one of the coordinate planes) going through the symmetry axis of the initial plasma cone. The thick contour shows the contact discontinuity at the edge of the region containing the material within the initial plasma bubble (this surface being tracked in the numerical simulation by labeling the plasma bubble with a passive scalar). Finally, in the $t = 7\,\mu s$ frame we also show the positions of the grid points resulting from the adaptive grid algorithm of the code. The scales of the axes are in mm, and the origin of the coordinate system coincides with the focal point (see Figure 2).

bodies of arbitrary shapes. This feature allows us to study the gasdynamics associated with volcanic explosions (for which the topography has to be considered), and other geophysical and aeronautical flows.

This work was supported by the DGAPA-UNAM IN-128098 (A.R.), IN110998 (M.V-M.) and IN102796 (R.N-G.) grants and the CONACyT 37253-E (A.R.) and 32531-T (R.N-G) grants.

REFERENCES

Falle, S. A. E. G., & Giddings, J. R. 1993, in Numerical Methods for Fluid Dynamics 4, ed. K. W. Morton & M. J. Baines (Oxford: Clarendon), 335
Falle, S. A. E. G., & Raga, A. C. 1993, MNRAS, 261, 573
Flower, D. R., & Pineau des Fôrets, G. 1999, MNRAS, 308, 271
Horváth, A., Ziegler, U. 1999, A&A, 349, 595
Klein, R. I., McKee, C. F., & Colella, P. 1994, ApJ, 433, 757
Lim, A. J., Rawlings, J. M. C., & Williams, D. A. 1999, MNRAS, 308, 1126
Lim, A. J., & Steffen, W. 2000, MNRAS, in press
Mellema, G., Raga, A. C., Cantó, J., Lundqvist, P., Balick, B., Steffen, W., & Noriega-Crespo, A. 1998, A&A, 331, 335
Raga, A. C., Mellema, G., & Lundqvist, P. 1997b, ApJS, 109, 517
Raga, A. C., Mellema, G., Arthur, S. J., Binette, L., Ferruit, P., & Steffen, W. 1999, RevMexAA, 35, 123
Raga, A. C., Noriega-Crespo, A., Cantó, J., Steffen, W., Van Buren, D., Mellema, G., & Lundqvist, P. 1997a, RevMexAA, 33, 73
Raga, A. C., & Williams, D. A. A&A, in press
Truelove, J. K., Klein, R. I., McKee, C. F., Holliman, J. H., Howell, L. H., Greenough, J. A., & Woods, D. T. 1998, ApJ, 495, 821
Young, T. R., & Boris, J. P. 1973, NRL Mem. Rep. 2611
Van Leer, B. 1982, ICASE Report No. 82–30
Villagrán-Muniz, M., & Navarro-González, R. 2000, Rev. Sci. Instrum., submitted
Williams, R. J. R. 1999, MNRAS, 310, 789

Alejandro C. Raga: Instituto de Astronomía, UNAM, Apartado Postal 70-264, 04510 México, D. F., México (raga@astroscu.unam.mx).
Rafael Navarro-González: Instituto de Ciencias Nucleares, UNAM, Apartado Postal 70-543, 04510 México, D. F., México (navarro@nuclecu.unam.mx).
Mayo Villagrán-Muniz: Centro de Instrumentos, UNAM, Apartado Postal 70-186, 04510 México, D. F., México (mayo@aleph.cinstrum.unam.mx).